

DETAILED DIAGNOSTICS OF AN X-RAY FLARE IN THE SINGLE GIANT HR 9024

PAOLA TESTA,¹ FABIO REALE,^{2,3} DAVID GARCIA-ALVAREZ,⁴ AND DAVID P. HUENEMOERDER¹

Received 2007 January 22; accepted 2007 March 9

ABSTRACT

We analyze a 96 ks *Chandra* HETGS observation of the single G-type giant HR 9024. The high flux allows us to examine spectral line and continuum diagnostics at high temporal resolution, to derive plasma parameters. A time-dependent one-dimensional hydrodynamic model of a loop with half-length $L = 5 \times 10^{11}$ cm ($\sim R_*/2$) and cross-sectional radius $r = 4.3 \times 10^{10}$ cm, with a heat pulse of 15 ks and 2×10^{11} ergs cm⁻² s⁻¹ deposited at the loop footpoints, satisfactorily reproduces the observed evolution of temperature and emission measure, derived from the analysis of the strong continuum emission. For the first time we can compare predictions from the hydrodynamic model with single spectral features, other than with global spectral properties. We find that the model closely matches the observed line emission, especially for the hot ($\sim 10^8$ K) plasma emission of the Fe xxv complex at ~ 1.85 Å. The model loop has $L/R_* \sim 1/2$ and aspect ratio $r/L \sim 0.1$, as typically derived for flares observed in active stellar coronae, suggesting that the underlying physics is the same for these very dynamic and extreme phenomena in stellar coronae independently of stellar parameters and evolutionary stage.

Subject headings: hydrodynamics — plasmas — stars: activity — stars: coronae — stars: flare — stars: individual (HR 9024) — X-rays: stars

Online material: color figures

1. INTRODUCTION

The first X-ray stellar surveys showed widespread presence of coronal emission in the cool half of the H-R diagram (see, e.g., Vaiana et al. [1981] for a review). Improved spatial and spectral resolution have provided us with more powerful tools for investigating the characteristics of the X-ray coronal activity in late-type stars and for exploring the underlying processes at work in stars with different stellar parameters and evolutionary stage.

X-ray observations of late-type stars show that coronal phenomena observed at close range on the Sun are common in late-type stars, although they occur on more extreme scales in very active stars. For instance, stars at higher activity levels have reached much higher temperatures and densities (e.g., Sanz-Forcada et al. 2002; Testa et al. 2004; Ness et al. 2004) than typically observed for solar coronal plasma. Analogously, coronal flares are routinely observed in late-type stars with characteristics similar to those observed in solar flares, e.g., fast rise and slow decay (e.g., Reale [2002] for a review), but at the same time, the flare frequency and intensity can be dramatically larger than observed on the Sun, with stellar X-ray luminosity increasing by orders of magnitude with respect to the quiescent level (e.g., Favata et al. 2000; Osten et al. 2007).

The analysis of light curves during flares provides us with insights into the characteristics of the coronal structures and therefore of the magnetic field (e.g., Schmitt & Favata 1999; Favata et al. 2000; Reale et al. 2004). Even though stellar flares are spatially unresolved, a great deal of information about the coronal heating and the plasma structure morphology can be inferred from detailed modeling of stellar flares; for instance, if enough

data statistics is available for moderately time-resolved spectral analysis, the study of the complete evolution of a flare allows us to infer whether the flare occurs in closed coronal structures (loops), what the size of these flaring structures is, whether continuous heating is present throughout the flare, and even constraints on the location and distribution of the heating (see Reale et al. [2004] and § 4.2 for a detailed discussion).

This work presents a detailed modeling of a large X-ray flare on the single evolved G1 III giant HR 9024, observed with the *Chandra* High Energy Transmission Grating (HETG). Most of the flare is observed, from the rise phase to the late decay, allowing us to constrain a detailed hydrodynamic simulation of the flaring structure. The analysis of this flare is especially interesting in the context of the X-ray activity of evolved giants. HR 9024 is an intermediate-mass star ($M_* \sim 2.9 M_\odot$) in the Hertzsprung gap that is in its initial rapid (< 1 Myr) phase of post-main-sequence evolution when it enters the cool region of the H-R diagram, and it develops a subphotospheric convective layer (see, e.g., Pizzolato et al. 2000). The intermediate-mass Hertzsprung gap giants are strong X-ray emitters ($L_X \sim 10^{31}$ ergs s⁻¹), while their main-sequence progenitors, late-B or early-A type, are X-ray-dark, lacking the fundamental ingredients to sustain X-ray activity, either magnetic dynamo, as in late-type stars, or strong winds, as in massive stars. The onset of an efficient convective layer, together with their typically fast rotation rates (due to the little if any loss of angular momentum in their main-sequence phase), is thought to generate a dynamo mechanism sustaining the X-ray activity of these evolved yellow giants. The young coronae of these stars are characterized by high temperature and density (e.g., Ayres et al. 1998; Testa et al. 2004), similar to low-mass active stars at the same high activity levels (e.g., Sanz-Forcada et al. 2002; Testa et al. 2004); on the other hand, there is evidence for significant differences, such as much lower coronal filling factors (Testa et al. 2004) and very limited flaring activity. The evolved intermediate-mass giants, both in the Hertzsprung gap and in the post-helium flash clump (the relatively long-lived, ~ 70 Myr, core helium-burning phase;

¹ Massachusetts Institute of Technology, Kavli Institute for Astrophysics and Space Research, Cambridge, MA 02139; testa@space.mit.edu.

² Dipartimento di Scienze Fisiche & Astronomiche, Sezione di Astronomia, Università di Palermo 90134 Palermo, Italy.

³ INAF-Osservatorio Astronomico di Palermo, 90134 Palermo, Italy.

⁴ Imperial College London, Blackett Laboratory, London, SW7 2AZ, UK; Harvard-Smithsonian Center for Astrophysics, Cambridge, MA 02138.

TABLE 1
STELLAR PARAMETERS

Parameter	Value	Source
Spectral type	G1 III
d	135 pc	SIMBAD
R	$13.6 R_{\odot}$	Singh et al. (1996)
M	$2.9 M_{\odot}$	Gondoin (1999)
$\log L_{\text{bol}}$	35.4 ergs s^{-1}	Flower (1996)
P_{rot}	23.25 days	Singh et al. (1996)

Ayres et al. 1999), show an extremely constant X-ray emission level (e.g., Haisch & Schmitt 1994; Gondoin 2003; Testa et al. 2004; Audard et al. 2004; Scelsi et al. 2004), and only a few flares have been observed on these sources (Haisch & Schmitt 1994; Ayres et al. 1999; this work).

The opportunity to derive a loop length from the analysis of the flare is interesting also in that it gives us an opportunity to probe the structuring of the corona, which in principle can be significantly different from dwarf star coronae. In fact, in these giants the gravity is considerably lower than for main-sequence late-type stars, therefore yielding a larger scale height, and possibly allowing very extended coronae (as suggested, for example, by Ayres et al. 2003) to develop. In the case of HR 9024, the surface gravity is only $\sim 0.02 g_{\odot}$, implying a scale height of about 3 stellar radii at 10^7 K ($30R_{*}$ at 10^8 K).

HR 9024 (HD 223460, OU And) is a moderately rotating ($v \sin i \sim 21 \text{ km s}^{-1}$; de Medeiros & Lebre 1992), chromospherically active single giant, not very well studied, even though it is a bright and nearby object ($d \sim 135 \text{ pc}$; Perryman et al. 1997). The stellar parameters are listed in Table 1. Several X-ray observations of HR 9024 exist, indicating high and constant X-ray luminosity of a few $\times 10^{31} \text{ ergs s}^{-1}$. Singh et al. (1996) analyzed *Röntgensatellit* (*ROSAT*) PSPC observations of chromospherically active stars and derived an X-ray luminosity $L_X \sim 4.3 \times 10^{31} \text{ ergs s}^{-1}$ in the 0.2–2.4 keV energy band; this translates to $L_X \sim 2.6 \times 10^{31} \text{ ergs s}^{-1}$ using the revised distance of 135 pc, instead of 175 pc, as assumed by Singh et al. (1996). This value is in good agreement with values obtained by Gondoin (2003) in the 0.3–2 keV range, from two short *XMM-Newton* observations of HR 9024 showing little, if any, variability: $L_X \sim 2.7 \times 10^{31} \text{ ergs s}^{-1}$ (Rev. 107; 6 ks exposure time) and $L_X \sim 2.3 \times 10^{31} \text{ ergs s}^{-1}$ (Rev. 200; 3 ks exposure time); the total X-ray luminosities in the 0.3–10 keV range are 3.8×10^{31} and $3.0 \times 10^{31} \text{ ergs s}^{-1}$, respectively.

Our approach here is to inspect the flare light curve and spectra and derive some quantities relevant to set up a loop hydrodynamic model and to constrain the initial parameters. The numerical solution of the hydrodynamic equations allows us to synthesize in detail the emission (by so-called forward modeling) as it would really be observed and therefore to compare directly to the data. This allows us to get feedback on the model and to refine the model parameters. After obtaining a good description of the global features, i.e., the light curve and the overall evolution of the temperature and total emission measure, the model will have constrained the loop length and aspect and the heating function. The comparison with the fine details of the data analysis will give us insight into the flare density and thermal structure and evolution and help us to interpret the results of the data analysis.

The paper is structured as follows. We describe the observations in § 2 and the methods for both the spectral analysis and the hydrodynamic modeling in § 3; in § 4 we present the results of our study, and in § 5 we draw our conclusions.

TABLE 2
PARAMETERS OF HETG OBSERVATION

Parameter	Value
ObsID	1892
Start	2001 Aug 11, 00:19:04
End	2001 Aug 12, 03:43:14
t_{exp}	95.7 ks
$\log L_X^a$	31.8 ergs s^{-1}
$\log L_{X,\text{peak}}^b$	32.1 ergs s^{-1}

^a From MEG spectrum, in the 2–24 Å range, averaged over the whole observation.

^b Peak X-ray luminosity obtained from the MEG spectrum integrated in the time interval 10–15 ks from the beginning of the observation.

2. OBSERVATIONS

We analyzed the *Chandra* High Energy Transmission Grating Spectrometer (HETGS; see Canizares et al. [2000, 2005] for a description of the instrumentation) observation of the X-ray-active single G1 giant HR 9024. The data were obtained from the *Chandra* Data Archive⁵ and have been reprocessed using standard CIAO 3.3 tools and analysis threads. Effective areas and line responses (ARFs and RMFs) were calculated using standard CIAO procedures.⁶ The characteristics of the HETG observation are listed in Table 2.

Figure 1 shows the *Chandra* High Energy (HEG) and Medium Energy (MEG) Gratings spectra for the $\sim 96 \text{ ks}$ observation of HR 9024. The spectrum is characterized by a strong continuum emission, indicating high-temperature plasma, as well as the unusually strong Fe xxv complex at $\sim 1.85 \text{ Å}$ ($\log T[\text{K}] \sim 7.8$) and the Ca xx resonance line at 3.02 Å ($\log T[\text{K}] \sim 7.7$); these characteristics are somewhat extreme when compared with the spectra of other very active stellar coronae (see, e.g., Testa et al. 2004). Other prominent features in the spectrum are the H-like and He-like lines of Si (~ 6.2 and 6.7 Å , respectively) and Mg (~ 8.4 and 9.2 Å) and the strong emission lines of highly ionized Fe around 11 Å .

The light curve of the summed HEG+MEG dispersed photons integrated in the 1.5–26 Å range, presented in Figure 2, shows clear variability: the X-ray emission level rises steeply at the beginning of the observation by a factor ~ 3 in about 15 ks; after a slow decay on a timescale of about 40 ks, the light curve rises again, peaking around 80 ks from the beginning of the observation. The light curves for a hard (1.5–12 Å) and a soft (12–26 Å) spectral band, also shown in Figure 2, indicate hardening of the spectrum corresponding to the two peaks of the emission, typical of stellar flares. The peak luminosity above $10^{32} \text{ ergs s}^{-1}$ is extremely high when compared with typical energies of stellar flares observed in active coronae of late-type stars.

3. ANALYSIS

Spectra were analyzed with the PINTofALE⁷ IDL⁸ software (Kashyap & Drake 2000). The high-resolution spectra provide several plasma diagnostics (temperature, density, abundances, and emission measure distribution) from the analysis of both continuum and emission lines and from the light curves in different spectral bands or in single lines. The high flux allows us to examine spectral line and continuum diagnostics at high temporal resolution.

⁵ See <http://cxc.harvard.edu/cda>.

⁶ See <http://cxc.harvard.edu/ciao/threads>.

⁷ See <http://hea-www.harvard.edu/PINTofALE>.

⁸ Interactive Data Language, Research Systems Inc.

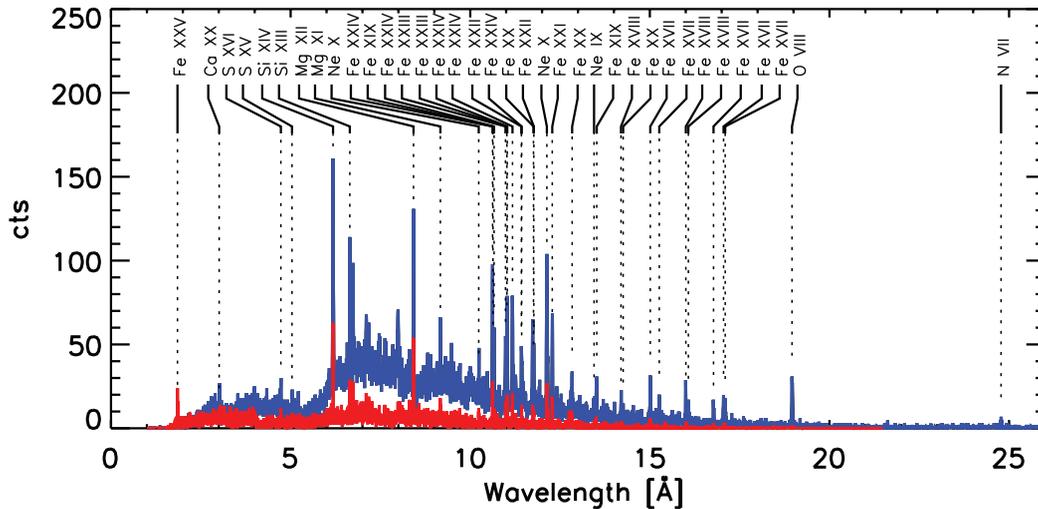


Fig. 1.—*Chandra* HEG (red) and MEG (blue) spectra obtained in a 96 ks observation of the single giant HR 9024. Line identification for many prominent spectral features is provided.

3.1. Spectral Analysis

Continuum emission.—The strong continuum emission in this spectrum provides us with constraints on the hot plasma on which it strongly depends. Specifically, the temperature and emission measure, EM, can be estimated through a fit of the continuum, and their evolution, probing the hottest plasma component, allows us to constrain the hydrodynamic model of the flaring structures (see §§ 3.2 and 4.2). In order to derive T and EM, we fit the continuum simultaneously in the HEG and MEG spectrum, selecting narrow spectral regions that can be assumed to be reasonably line-free on the basis of predictions of the atomic databases APED (Smith et al. 2001) and CHIANTI (Dere et al. 1997; Landi et al. 2006). We fit the continuum with an isothermal model computed in PINTofALE using CHIANTI and convolved with the HETG spectral response. This model contains all the contributions to the continuum (free-free, free-bound, and two photon); however, at high temperature ($\log T[\text{K}] \gtrsim 7.5$), as observed in this spectrum, the bremsstrahlung continuum is by far the dominant process for the formation of the continuum.

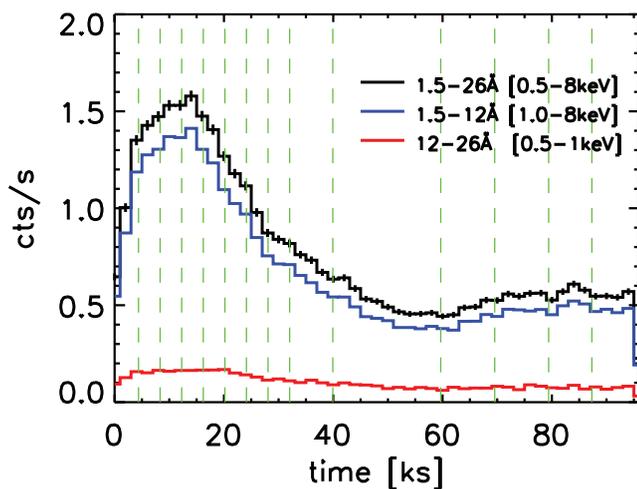


Fig. 2.—Light curve obtained as the sum of total counts of HEG and MEG dispersed spectra, using a temporal bin size of 2 ks. Light curves in hard (blue) and soft (red) spectral bands are shown. The vertical green dashed lines mark the time intervals selected for the temporally resolved spectral analysis and the hydrodynamic modeling (see § 3).

The line-free spectral regions used for the fit are 2.00–2.95, 4.4–4.6, 5.3–6.0, 7.5–7.8, 12.5–12.7, and 19.1–20 Å. The fit also provides an estimate for EM from the normalization parameter. The analysis of the strong continuum emission allows us to derive the evolution of the temperature and emission measure during the flare with high temporal resolution. The time intervals chosen for this analysis are shown in Figure 2 superimposed on the light curve; they have been selected in order not only to have high temporal resolution, but also good constraints on the plasma parameters.

Line emission.—The line fluxes are determined using the technique of spectral fitting described in Testa et al. (2004). The measured line fluxes have been used to reconstruct the emission measure distribution, determine the abundances (§ 4.1), and compare with the results of the hydrodynamic model (§ 4.2).

Abundances and emission measure distribution.—The emission measure distribution, $EM(T)$, is derived through a Markov chain Monte Carlo analysis using the Metropolis algorithm (MCMC[M]; Kashyap & Drake 1998) on a set of line flux ratios, as in García-Alvarez et al. (2006). O lines are the coolest lines used, and Ar lines are the hottest, covering a temperature range $\log T[\text{K}] \sim 6.2$ –7.8. Coronal abundances are evaluated on the basis of the derived $EM(T)$: the abundance is a scaling factor in the line flux equation to match the measured flux (García-Alvarez et al. 2006).

3.2. Hydrodynamic Modeling

Inspection of the light curve, the evolution of the temperature, and the integrated emission measure (EM) during the flare allows us to set up a detailed model of the flaring structure(s) (Reale et al. 2004), as described in detail in § 4.2. We derive the temperature and EM parameters through the analysis of the continuum emission as described above (§ 3.1), the continuum emission being strong and probing the hottest plasma.

The one-dimensional hydrodynamic model solves time-dependent plasma equations with detailed energy balance (Peres et al. 1982; Betta et al. 1997), with a time-dependent heating function defining the energy release that triggers the flare (see, e.g., Reale et al. 1997, 2004). The coronal plasma is confined in a closed loop structure, where plasma motion and energy transport occur only along magnetic field lines. For the initial atmosphere, we assume a loop in hydrostatic equilibrium and detailed energy

TABLE 3
MEASURED FLUXES OF THE SPECTRAL LINES USED IN OUR ANALYSIS,
DURING THE FLARE AND OUTSIDE THE FLARE

Ion	λ_{obs} (Å)	$\log T_{\text{max}}^a$ (K)	Flux _{flare}	Flux _{quiesc}	Use ^b
Fe xxv	1.853	7.8	94 ± 19	13.5 ± 8.4	M
Fe xxv	1.864	7.8	49 ± 16	16.0 ± 8.4	M
Ca xx	3.024	7.7	21.7 ± 6.8	<4.4	S
Ca xix	3.187	7.4	18.7 ± 6.4	5.8 ± 3.7	S
Ar xviii	3.734	7.6	14.1 ± 7.0	4.2 ± 3.6	S
Ar xvii	3.945	7.3	13.5 ± 6.7	4.7 ± 4.0	S
S xvi	4.729	7.4	20.3 ± 8.7	10.8 ± 5.7	S
S xv	5.041	7.2	30 ± 11	9.5 ± 6.0	S
Si xiv	6.183	7.2	82.9 ± 6.0	42.2 ± 3.6	SM
Si xiii	6.648	7.0	33.1 ± 4.2	25.7 ± 3.0	S
Al xiii	7.170	7.1	15.9 ± 4.5	8.1 ± 3.1	S
Al xii	7.759	6.9	6.2 ± 3.8	5.6 ± 3.1	S
Mg xii	8.422	7.0	80.7 ± 6.4	47.5 ± 4.5	SM
Mg xi	9.168	6.8	31.0 ± 4.7	15.2 ± 2.8	S
Ne x	12.132	6.8	142. ± 12.	113. ± 9.3	S
Fe XXI	12.284	7.0	79. ± 11.	53.5 ± 7.2	S
Ne ix	13.448	6.6	20. ± 10.	22.6 ± 7.4	S
Fe xviii	14.201	6.9	50. ± 15.	30.1 ± 9.1	S
Fe xvii	15.012	6.7	107. ± 22.	43. ± 13.	S
O viii	18.965	6.5	270. ± 42.	179. ± 29.	S
O vii	21.602	6.3	51 ± 44.	<25	S
N vii	24.778	6.3	65. ± 50.	72. ± 40.	S

Flux units are 10^{-6} photons $\text{cm}^{-2} \text{s}^{-1}$.

^a Temperature of maximum formation of the line.

^b Use indicates whether the line was used in the spectral analysis (S), for the emission measure reconstruction and abundance determination, and whether the feature was used for the direct comparison with the loop model (M; see § 4.2).

balance (Serio et al. 1981) with maximum temperature (at the apex) $T_{\text{max}} = 2 \times 10^7$ K; after a very short time, the initial conditions do not influence the evolution of the plasma much.

The outputs of the hydrodynamic simulations are distributions of temperature and density along the loop sampled at regular times throughout the flare evolution. From these plasma

parameters we synthesize the corresponding HETG spectrum of each (isothermal) plasma volume along the loop at each given time, using isothermal models folded with the HETG spectral response. We then integrate along the loop to obtain the overall HETG spectrum of the multithermal plasma in the flaring structure.

4. RESULTS

4.1. Emission Measure Distribution and Abundances

As a first step, we carry out an analysis of the spectrum to study the global characteristics of thermal distribution and abundances. To obtain this information, we need strong lines from different elements covering a wide temperature range. We have to integrate on time intervals long enough to have good photon statistics for each line. This limits our temporal resolution, and we are not able to derive $EM(T)$ and abundances in several portions of the flare, but only in two different portions of the observation: during the flare (i.e., using the spectrum integrated over the first 40 ks of the observation) and outside the flare (40–96 ks). We note that hereafter we label the parameters derived outside the flare as “quiescent,” even though the corona seems to undergo another dynamic event. This second flare is on a smaller scale with respect to the first one. The analysis of the abundances is also useful for the synthesis of the spectra from the results of hydrodynamic modeling and a consistent comparison with the data.

Table 3 lists the fluxes of the spectral lines used for this analysis, measured in the two phases of flare and quiescence. Figures 3 and 4 show the emission measure distribution and the coronal abundances derived from the flare spectrum and from the quiescent emission. The thermal distribution of the coronal plasma in HR 9024 appears dominated by hot (i.e., typical of flaring structures) plasma both during and outside the period of the flare. Hot emission ($T \gtrsim 2 \times 10^7$ K) was also found from the analysis of two very short (6 and 3 ks) *XMM-Newton* observations of HR 9024 when the corona seems to be in its quiescent state (Gondoin 2003). The main difference between the $EM(T)$ of flare and quiescence is at the hot end of the temperature range, i.e., for

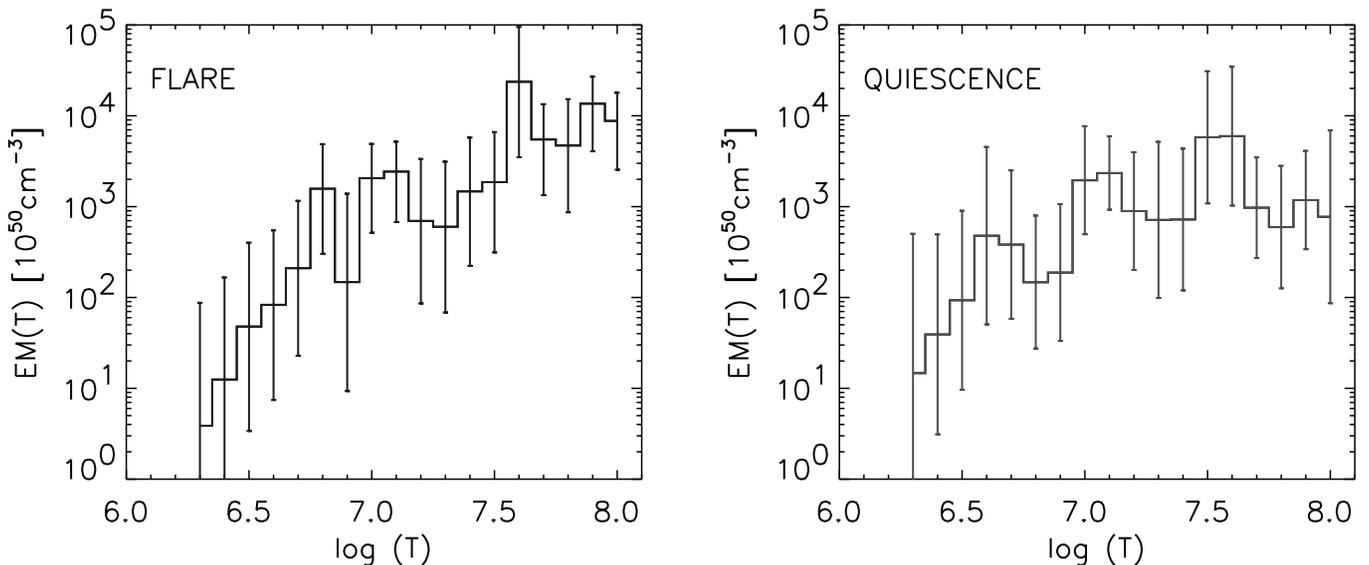


FIG. 3.—Emission measure distribution derived from the flare portion of the spectrum (0–40 ks; left) and from the spectrum outside the flare (40–96 ks; right). The comparison shows that the main difference between flare and quiescent emission resides in the hot end of the temperature range, i.e., for $\log T[\text{K}] \gtrsim 7.5$, where the $EM(T)$ of the flaring plasma is about 1 order of magnitude higher than the $EM(T)$ of the plasma outside the flare. [See the electronic edition of the Journal for a color version of this figure.]

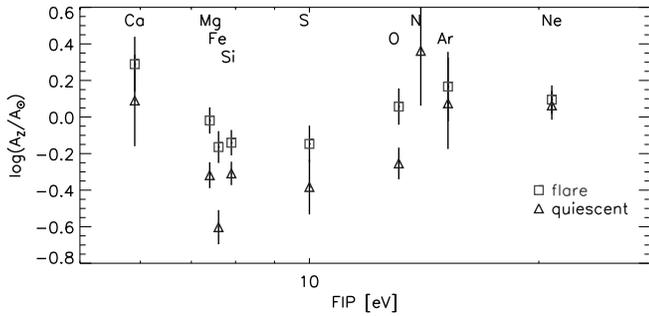


FIG. 4.—Coronal abundances relative to solar abundances (Asplund et al. 2005) as a function of the first ionization potential (FIP) derived for HR 9024 during the flare (squares) and the quiescent (triangles) phases. [See the electronic edition of the Journal for a color version of this figure.]

log T [K] ≥ 7.5 , where the EM(T) of the flaring plasma is about 1 order of magnitude higher than the EM(T) of the plasma outside the flare. The EM(T) derived for HR 9024 presents interesting characteristics when compared to other active coronae. Specifically, the EM(T) of HR 9024 is characterized by a rather shallow slope, similar to the slope of hydrostatic loop models [EM(T) $\propto T^{3/2}$; Rosner et al. 1978], whereas for several active coronae there is increasing evidence of steep, almost isothermal, emission measure distributions, possibly indicating the dynamic nature of the coronal loops composing them (Testa et al. 2005). For instance, such steep EM(T) are derived for other giants, e.g.,

the Hertzsprung gap giant 31 Com (Scelsi et al. 2004), the clump giants β Cet, (Sanz-Forcada et al. 2002), Capella (Dupree et al. 1993), and other active stars (e.g., Griffiths & Jordan 1998; Drake et al. 2000; Sanz-Forcada et al. 2002).

The coronal abundance pattern observed in HR 9024 (Fig. 4) presents characteristics similar to other intermediate-mass giants, i.e., little or no first ionization potential (FIP) effect (García-Alvarez et al. 2006). All abundances are plotted relative to the solar mixture of Asplund et al. (2005), as photospheric abundances for HR 9024 have not been determined. We find significant changes in the coronal abundances during the flare with respect to the quiescent phase: all elements appear to be enhanced, except possibly Ne, and the Fe abundance in particular is found to increase by almost a factor of 3. Both the abundances and EM(T) for HR 9024 have also been derived by Nordon & Behar (2007), and their findings are in agreement with the results presented here.

4.2. Flaring Loop Modeling

High-level diagnostics of the flare can be obtained from detailed hydrodynamic modeling of the flaring plasma (Reale et al. 1988, 2004). The analogy of stellar to solar flares suggests that, like solar flares, stellar flares mainly occur in closed magnetic structures (coronal loops). It is customary to assume that the bulk of the flare involves a single coronal loop, which can be then investigated by analyzing the flare characteristics.

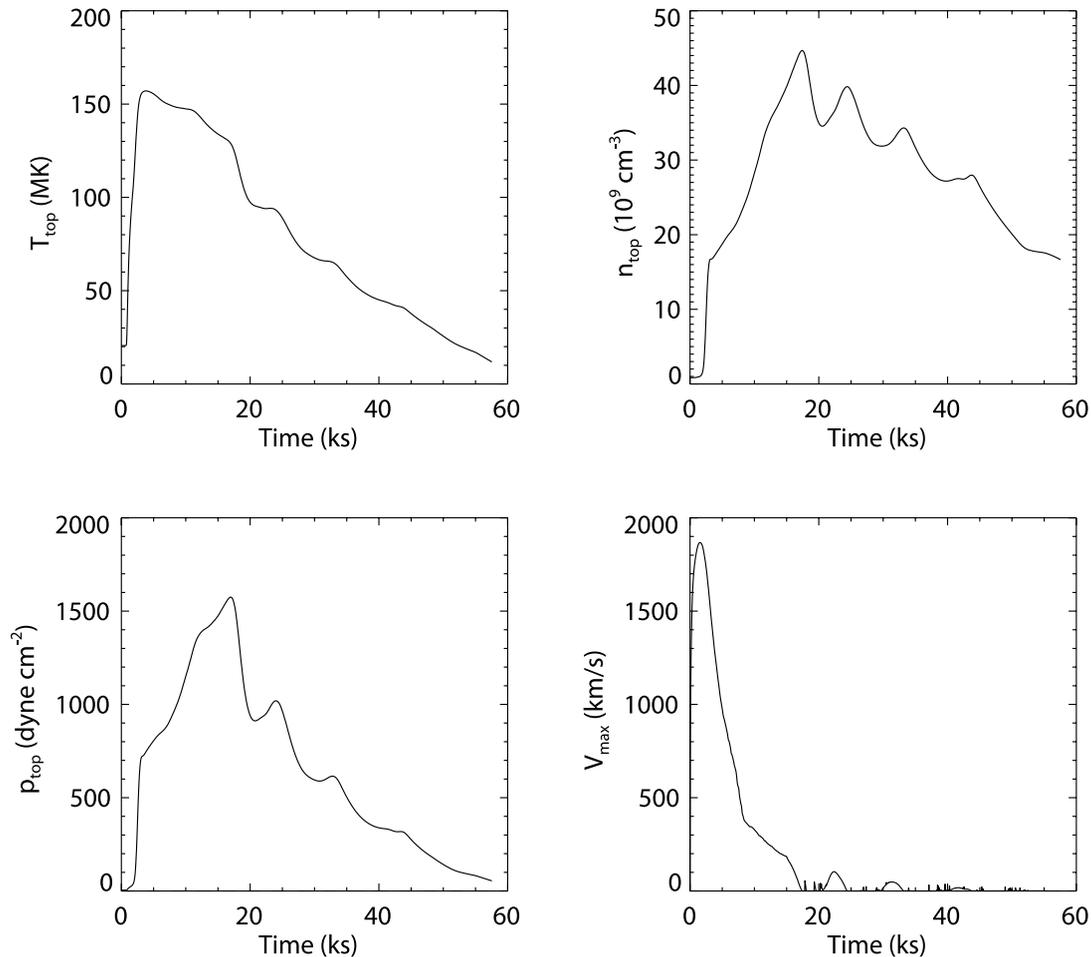


FIG. 5.—Evolution of the temperature, density, and pressure at the loop apex and of the maximum plasma velocity according to the loop hydrodynamic model of the flare.

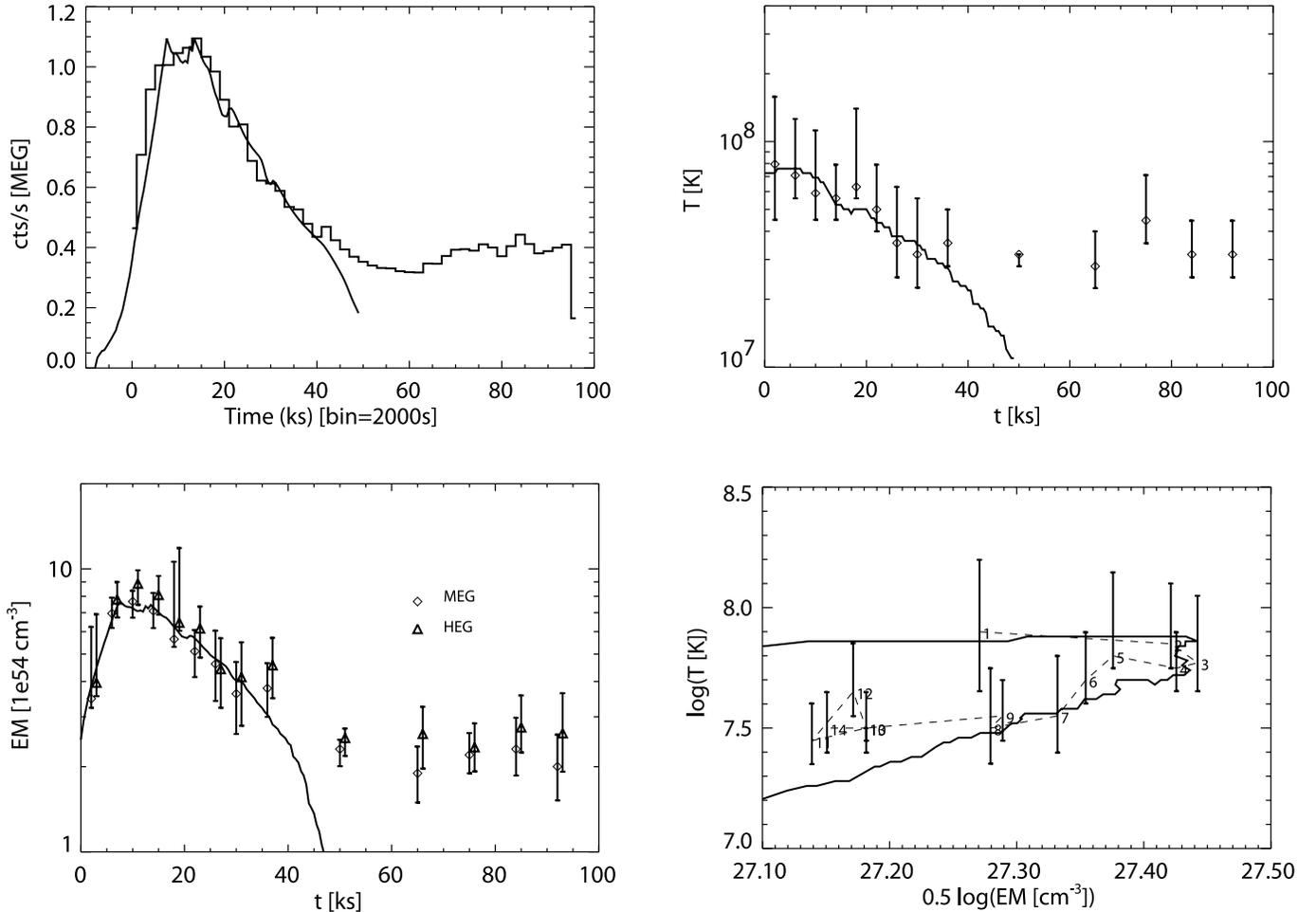


FIG. 6.— Comparison of the observed light curve (*top left*), T (*top right*), EM (*bottom left*), and T - n (*bottom right*) evolution, with the corresponding quantities synthesized from the hydrodynamic loop model (*thick solid lines*) characterized by half-length $L = 5 \times 10^{11}$ cm and footpoint impulsive heating. Evolution of temperature and emission measure (*top right and bottom left*) are derived from the fit with isothermal models to the continuum emission in the spectra integrated over the time intervals shown in Fig. 2.

The plasma confined in coronal loops can be described as a compressible fluid that moves and transports energy exclusively along the magnetic field lines. We can then model a flare by solving the time-dependent hydrodynamic equations in the coordinate along the loop, assuming an appropriate transient input heating function. The main model parameters include the loop length and the intensity, distribution, and duration of the heat pulse. These parameters are constrained by the observed flare evolution, in particular in the decay phase, and by parameters derived from the data analysis, such as the temperature and emission measure at flare maximum and the timing of the maximum. Scaling laws, such as those shown in Reale et al. (1997), help us constrain the loop length from the light-curve decay time and the maximum flare temperature:

$$L_9 = \frac{\tau_X \sqrt{T_7}}{120f(\zeta)}, \quad (1)$$

where L_9 is the loop half-length (10^9 cm), τ_X is the decay time of the light curve, T_7 is the flare temperature (10^7 K), and the correction factor $f(\zeta) \geq 1$, which takes into account possible significant heating during the decay, which might make the decay slower.

Other parameters, such as the loop initial atmosphere, or, for low-gravity stars, the stellar surface gravity, have much less in-

fluence on the flare evolution. We compute the evolution of the loop plasma by solving the time-dependent hydrodynamic equations of mass, momentum, and energy conservation for a compressible plasma confined in the loop (Peres et al. 1982; Betta et al. 1997), including the relevant physical effects, such as the plasma thermal conduction and radiative losses. The gravity component along the loop is computed assuming a radius $R_* = 3 R_\odot$ and a surface gravity $g_* = 0.1 g_\odot$.

We numerically integrate the equations over a time range of 50 ks. From the density and temperature distribution of the plasma along the model loop, we synthesize the expected plasma X-ray model spectrum and finally convolve with the *Chandra* MEG spectral response to produce synthetic count spectra as described in § 3.2.

The flare light curve integrated in the whole *Chandra* MEG band resembles quite closely the X-ray light curves of flares recently observed on pre-main-sequence stars (Favata et al. 2005). For this reason, we have assumed as a first set of parameters the same values that best describe a specific flare observed in the Orion region, i.e., a loop with constant cross section and half-length $L = 10^{12}$ cm, symmetric about the loop apex. The flare simulation is triggered by injecting a heat pulse in the loop that is initially at a temperature of ~ 20 MK. Two heat pulses are deposited with a Gaussian spatial distribution of intensity $10 \text{ ergs cm}^{-3} \text{ s}^{-1}$ and width 10^{10} cm (1/100 of the loop half-length) at a distance

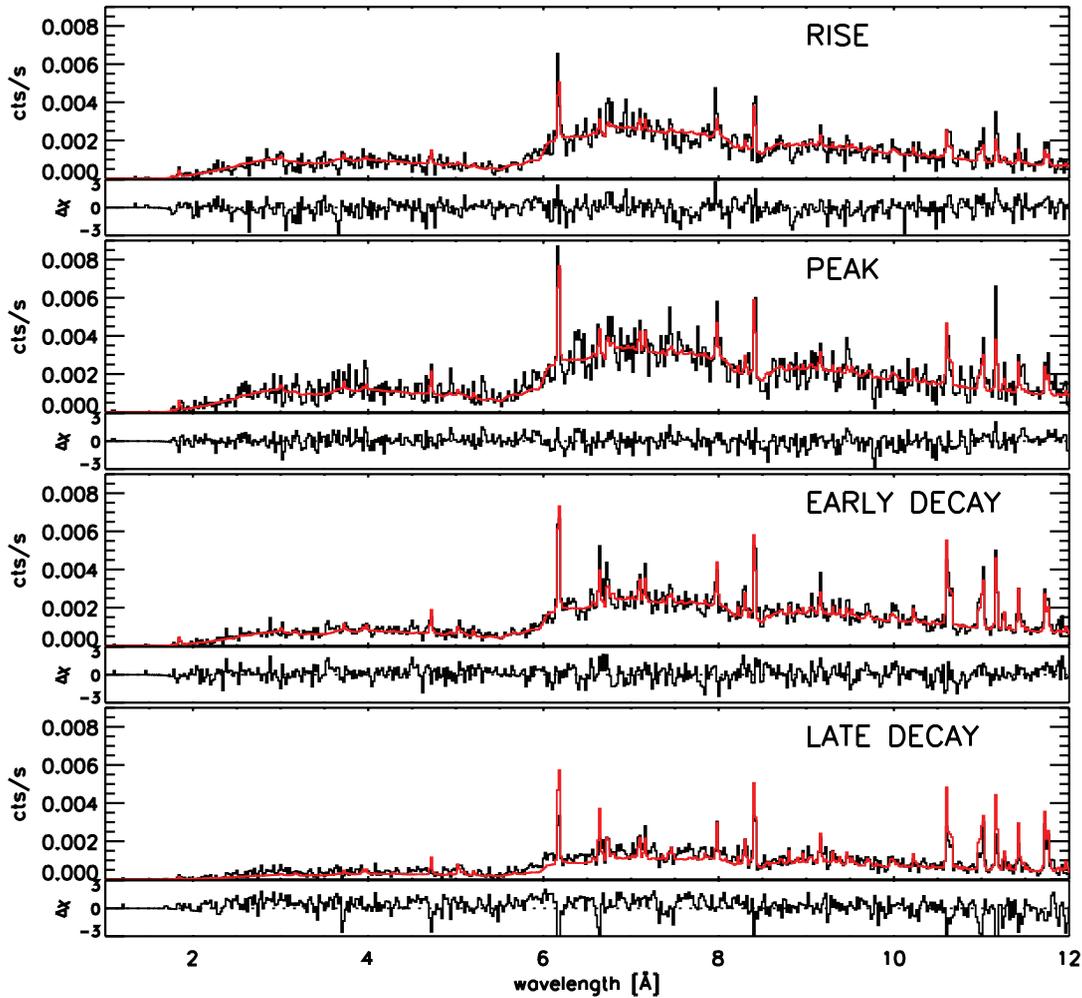


FIG. 7.— Comparison of the HR 9024 MEG spectrum (*black histogram*) and the MEG spectrum synthesized from the hydrodynamic model (*red histogram*) in four different phases of the flare. *From top to bottom*: Rise (0–10 ks from beginning of observation), peak (10–15 ks), early decay (15–30 ks), and late decay (30–45 ks). Spectra are shown in counts per second, and for better readability we split the spectral range in two plots showing the spectral range 1.5–12 and 12–22 Å, respectively. The small panel below each plot shows the χ residuals.

of 2×10^{10} cm from the footpoints, i.e., very close to them (Reale et al. 2004). After 20 ks, the heat pulses are switched off completely. With the above parameters, the light curve is reproduced with good accuracy, but we have noticed that the temperature values obtained from fitting the spectra with isothermal plasma emission models are significantly higher than those derived from the data throughout the flare evolution (Testa et al. 2006). Therefore, we have refined the model parameters to improve the fitting: we have reduced the input heating enough to account for the desired temperature decrease. From equation (1), in order to maintain the same decay time, a temperature reduction implies a shorter loop length. After this feedback, we have obtained best results with a loop half-length $L = 5 \times 10^{11}$ cm (half as long as before) and a heat pulse of $4 \text{ ergs cm}^{-3} \text{ s}^{-1}$ (peak volumetric heating) lasting 15 ks (5 ks less than before). The total energy flux rate is $2.0 \times 10^{11} \text{ ergs cm}^{-2} \text{ s}^{-1}$.

The computed evolution largely resembles the evolution computed for other stellar flares, although on larger scales than for typical flares observed in coronae of late-type stars (e.g., Reale et al. 2004). Figure 5 shows the evolution of the temperature, density, pressure at the apex of the loop, and maximum plasma velocity. The heat pulses make the loop plasma heat rapidly (~ 3 ks) at temperatures about 150 MK and expand

dynamically upward from the chromosphere at speeds about 1800 km s^{-1} to reach the loop apex, also in about 3 ks. After this first impulsive phase, the temperature slowly decreases to about 130 MK while the heat pulse is on, and the evaporation of plasma from the chromosphere, which brings the density increase shown in Figure 5, continues substantially, but less dynamically, with plasma speeds below 500 km s^{-1} after 9 ks, when the plasma pressure becomes higher than $1000 \text{ dynes cm}^{-2}$. The plasma pressure and density reach their peak, respectively, of $1500 \text{ dynes cm}^{-2}$ and $4.5 \times 10^{10} \text{ cm}^{-3}$ slightly (about 3 ks) later than the end of the heat pulse. Then they begin to decrease gradually with significant quasi-periodic fluctuations, while the temperature initially drops and then decreases more gradually.

Figure 6 shows the integrated light curve, assuming a loop cross-sectional radius of 4.3×10^{10} cm, i.e., 8% of the loop half-length. The spectra obtained from the loop modeling have also been fit with isothermal models. The resulting evolution of the emission measure, the temperature, and the T versus EM diagram are shown in the figure. A visual comparison of the model results with the data and the data-fitting results indicates that the loop simulation results are in good agreement with the data.

The dynamic model described above closely matches the evolution of temperature and emission measure derived from the

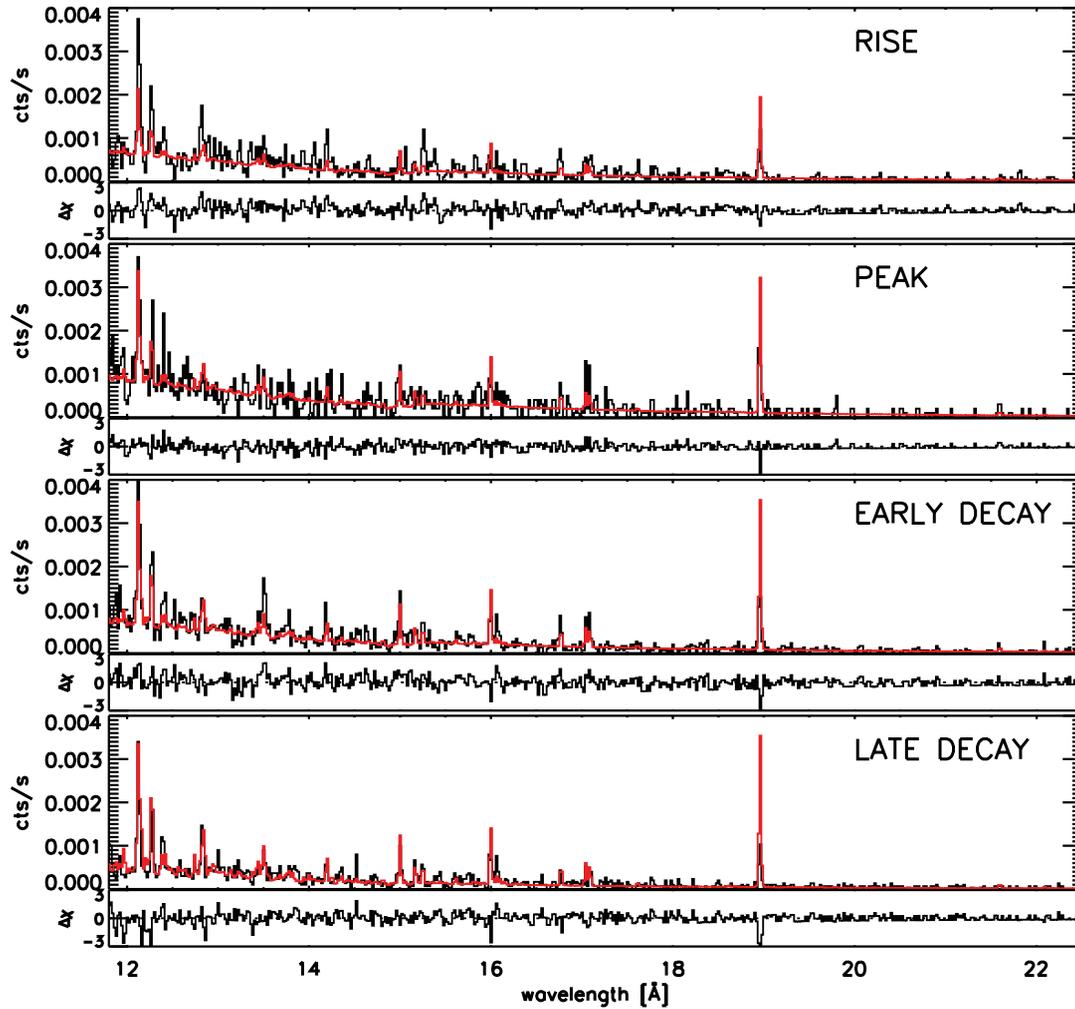


FIG. 7—Continued

continuum emission, and the light curve integrated over the entire wavelength range. The high-quality data allow us to test the model and perform a detailed comparison of its characteristics with the observations. In Figure 7 we compare the MEG spectra synthesized from the model with the observed spectra in four different phases of the flare: rise (0–10 ks from beginning of observation), peak (10–15 ks), early decay (15–30 ks), and late decay (30–45 ks). Figure 7 shows generally good agreement of the model spectra with the observations; however, some systematic discrepancies are observed. For example, in the spectrum of the late decay phase several lines, such as the Si XIV Ly α (~ 6.2 Å), the hot Fe lines around 11 Å, and the O VIII Ly α (~ 19 Å), are overpredicted. There are several factors that may determine these departures from the observations. For instance, the abundances used for synthesizing the model spectrum are the ones derived from the flare spectrum and are kept fixed. Since we observe significant changes in the abundances after the flare (§ 4.1), they may change on short timescales and affect the emission in the spectral lines. Another process, not taken into account in our modeling, that might affect the emission in the lines on short timescales is nonequilibrium ionization; however, this effect is expected to be relevant only at the very beginning of the flare (see e.g., Orlando et al. 2003). Furthermore, in our simulation, we assume that all the observed emission comes from the flaring structure; i.e., the emission of the quiescent corona (or of

other secondary flaring structures) is assumed to be negligible, whereas it could in fact contribute significantly to the “cool” [$\log T$ ([K]) $\lesssim 7.2$] lines at least, as suggested by the derived emission measures during flare and quiescence (Fig. 3).

The high quality of the data allows us to test the model to a much higher level of detail than before, for instance, by allowing a direct comparison with the light curves in single spectral features. The evolution in very hot spectral features emitted at the bulk plasma temperature of the flaring loop (i.e. $\log T$ [K] > 7.5) would represent more meaningful tests for the model. However, there are only a few very hot lines present in the spectrum (e.g., Fe XXV and Ca XX), and only the Fe XXV complex has enough signal to provide temporal resolution. Besides Fe XXV, we selected two other emission lines with high enough flux, Si XIV and Mg XII Ly α lines, and derived their light curves using the same time intervals used for the analysis of the continuum and marked in Figure 2. Figure 8 compares the light curves in these spectral features derived from the observations with those synthesized from the hydrodynamic simulation, assuming a loop cross-sectional radius $r = 4.8 \times 10^{10}$ cm. The line fluxes for Si XIV and Mg XII are obtained from the fit to the spectra integrated in each time interval. For the Fe XXV complex, the lower signal-to-noise ratio does not constrain the fit; however, since in the relevant wavelength range the continuum emission is rather small with respect to the line emission, we use the light curve integrated

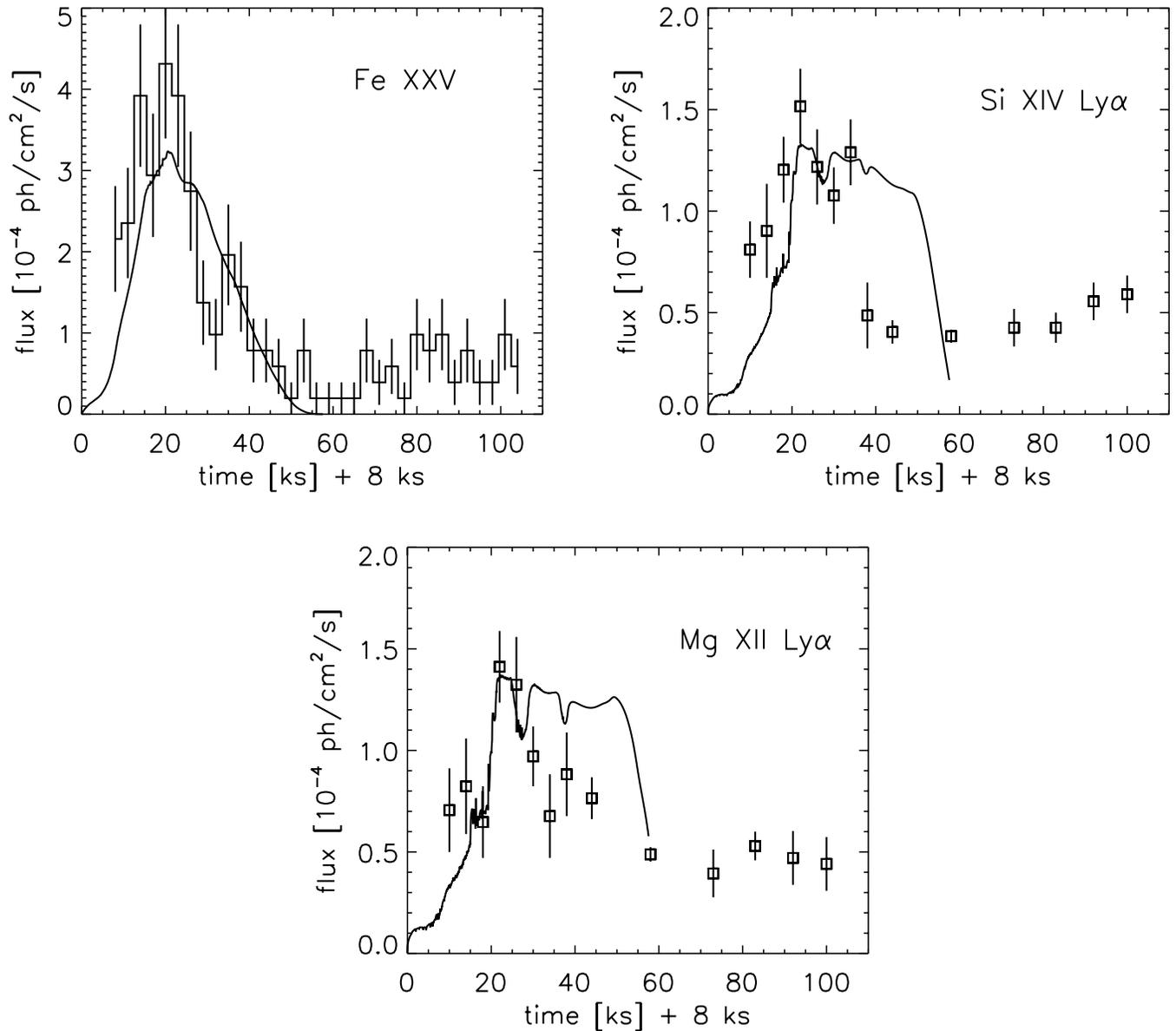


FIG. 8.—Light curves derived from HETG spectra in selected spectral features (*histograms with error bars*) compared with the prediction from the hydrodynamic model (*thick solid line*), assuming a loop cross-sectional radius 4.8×10^{10} cm.

in a small wavelength range (1.83–1.89 Å) using a 3 ks temporal bin.

The model reproduces extremely well the observed temporal behavior of the Fe xxv line complex. The light curves of Si xiv and Mg xii derived from the observation and from the model lie close to each other up to the peak of the flare. After the peak the observed emission in the two lines exhibits the dramatic drop predicted from the model, but on much shorter timescales, anticipating the model by slightly more than 10 ks. Other than the effects discussed above, we can identify another possible cause of this discrepancy. In the model of the flaring loop, the plasma contributing most to these “cool” lines ($\log T[\text{K}] \sim 7.0\text{--}7.2$) is located in the transition region of the loop, that is, the region where the plasma temperature and density steeply change from the dense and cool chromosphere to the hot and rarefied coronal portion of the loop. In this region some models predict an opening of the magnetic flux tube that could have a substantially larger cross section in the corona than in the low region

connecting it to the photosphere (e.g., Gabriel 1976; Schrijver et al. 1989; Litwin & Rosner 1993; Ciaravella et al. 1996). In this possible scenario, the emission of the flaring structure in these cool lines would be substantially reduced, and the resulting excess would therefore be attributed to the background corona or to nearby secondary flaring structures (e.g., Betta et al. 2001).

Finally, we compared the emission measure distribution of the loop model with the $EM(T)$ derived from the flare spectrum. Figure 9 shows that for the emission measure distribution the model predictions are also in very good agreement with the observations. This agreement is a further indication of the validity of the single-loop model for this flare and, on the other hand, of the EM inversion method. In our modeling of the X-ray emission during the flare, we assume any persistent quiescent emission to be negligible. As mentioned in § 4.1, the *Chandra* observation does not provide a good determination of the quiescent emission, as outside the large flare constituting the focus of our analysis the corona is undergoing another significant, although

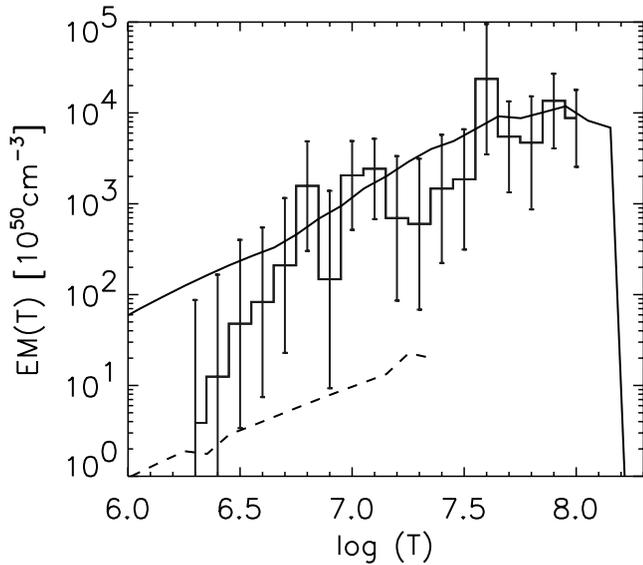


FIG. 9.—Comparison of emission measure distribution derived from the flare spectrum (histogram with error bars) with the $EM(T)$ of the hydrodynamic loop model (thick solid line). The dashed line shows the $EM(T)$ of the initial static loop with maximum temperature of 20 MK. [See the electronic edition of the *Journal* for a color version of this figure.]

smaller, dynamic event (its average, $L_X \sim 4.2 \times 10^{31}$ ergs s^{-1} , is about twice the luminosity value of other X-ray observations; see §§ 1 and 5). Other X-ray observations of this corona suggest that the quiescent emission is in fact negligible to a large extent with respect to the large, hot flare observed with *Chandra* (see § 5).

5. DISCUSSION AND CONCLUSIONS

Our analysis has shown that the observed evolution of the very hot coronal emission of the single giant HR 9024 is reproduced extremely well by a model characterized by a loop of semilength $L = 5 \times 10^{11}$ cm ($\sim R_*/2$) and impulsive footpoint heating triggering the flare. The heating pulse lasts 15 ks, and it is shifted by 8 ks before the beginning of observation. The peak volumetric heating is 4 ergs $cm^{-3} s^{-1}$, with a corresponding total heating rate $\approx 10^{33}$ ergs s^{-1} . The detailed analysis of the plasma evolution in the temperature-density diagram (Fig. 6) put tight constraints on the flare morphology and the characteristics of the heating. The delay of the EM peak with respect to the temperature peak indicates that the X-ray-emitting plasma is confined in a closed structure, whereas in nonconfined coronal flares the EM evolves simultaneously with the temperature, as shown by the analysis of hydrodynamic models (Reale et al. 2002). The steep slope of the decay path in the temperature-density diagram implies that after the initial phase, when the energy is released, the loop undergoes a pure cooling evolution, and no additional heating is needed to explain the evolution of the flaring plasma.

As discussed in § 4.2, the initial phases of the flare are very dynamic, and the plasma fills up the loop, expanding upward at very high speed, reaching ~ 1800 km s^{-1} . After about ~ 10 ks, therefore, corresponding to the start of the *Chandra* observation (considering the shift of 8 ks between the energy release and the start of the observation), the plasma speed rapidly decreases; however, during the first 5–10 ks of the observation, plasma flows with speeds up to a few $\times 100$ km s^{-1} are present. Such speeds can in principle be resolved by HETG. The plasma characterized by such high speed is at a temperature above 60 MK;

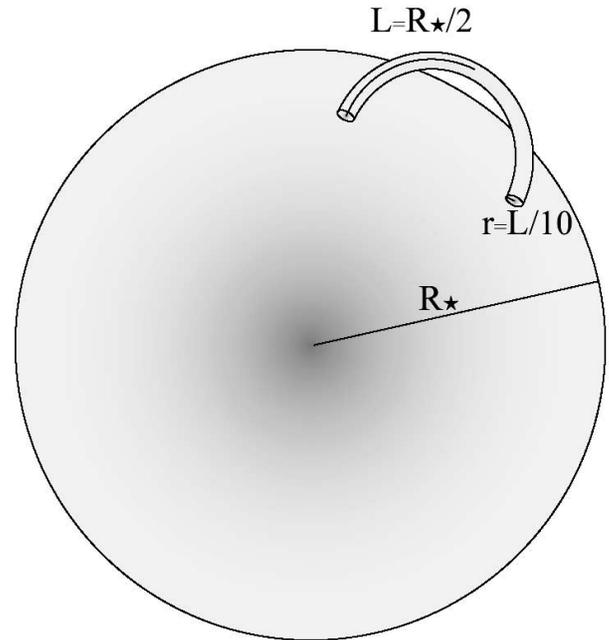


FIG. 10.—Sketch showing the geometry of the flaring loop of HR 9024 as derived from the hydrodynamic modeling of the flare; R_* is the stellar radius, L is the loop semilength, and r is the cross-sectional radius of the loop.

therefore, in order to investigate these speeds using Doppler shifts, we have to search for shifts in very hot lines. However, such hot lines, e.g., Ca xx, are at low λ , where the effective area is low and the instrument is not very sensitive. We searched for shifts in the Ca xx line, but we did not detect any significant shift. We note that, even if the instrument sensitivity were not a limiting factor, the detection of line shifts is expected only for a preferential orientation of the loop with respect to the line of sight.

The high photon statistics of the HETG data allowed us to derive light curves in a few relevant hot lines and, for the first time for a stellar flare, they could be compared in detail to those predicted by a hydrodynamic model (see Peres et al. [1987] and Betta et al. [2001] for analogous comparisons for a solar flare). On a more general level, we also compared the distributions of emission measure obtained from the data analysis and the flare loop model and found good agreement. The shape of the EM distribution is quite typical of a single coronal loop (e.g., Peres et al. 2000) and different from those found for active stars (e.g., Sanz-Forcada et al. 2002; Testa et al. 2005; Cargill & Klimchuk 2006).

From the normalization of the model light curves, we derive an estimate of the loop cross section and therefore of its aspect ratio, $\alpha = r/L$. We note that the loop cross-sectional radius, r , is a free parameter for which we can obtain independent estimates from the normalization of the different light curves: (1) integrated MEG-dispersed counts, (2) EM derived from the analysis of the continuum (Fig. 6), and (3) fluxes of spectral features (Fig. 9), therefore providing a cross-check of the consistency of our model. The obtained values $r = 4.9 \times 10^{10}$, 4.3×10^{10} , and 4.8×10^{10} cm, respectively, all agree within 15%, and they imply a loop aspect ratio $\alpha \sim 0.09$. Figure 10 shows a sketch of the morphology of the flaring structure, inferred from our modeling of the observed *Chandra* HETG spectra.

As mentioned in § 4.2, the loop model reproducing the observation has roughly the same parameters as models satisfyingly

reproducing other large flares, specifically the flares observed in pre-main-sequence stars (Favata et al. 2005). However, the derived loop parameters reveal some dissimilarity, possibly indicating fundamental differences between the processes at work in the two cases. The flaring loop reproducing the flare on HR 9024 is characterized by loop semilength $L \sim R_*/2$ and aspect ratio $r/L \sim 0.1$, as typically found for low-mass stars and the Sun. In contrast, the modeling of the flare on the pre-main-sequence stars, in particular the detailed model for COUP source 1343, yields a very large loop semilength corresponding to several stellar radii, with a much smaller aspect ratio $r/L \sim 0.02$ (Favata et al. 2005). These findings suggest that HR 9024 is characterized by a “normal” corona, while in the young stars showing evidence of elongated X-ray-emitting structures, possibly connecting the star to the disk, profoundly different processes may be at work.

Large flares such as the one observed in HR 9024 are very unusual in single intermediate-mass giants, and only a few such events have been studied in detail. This study thus allowed us to investigate the flaring activity in a single giant and provided us with a powerful tool to derive the size of its coronal structures. Even though the flaring structure modeled here is not necessarily representative of the typical coronal structures in X-ray-active giants, as discussed above, its characteristics are consistent with the presence of a corona with properties typical of active coronae, but scaled up to the larger stellar radius. The coronal properties derived through X-ray observations of these active giants might suggest a possible interpretation for the low frequency of flares. There is some evidence of very low coronal surface filling factors ($\leq 10^{-4}$) for these active giants, as suggested from density analysis (e.g., Testa et al. 2004). Considering the interaction of magnetic fields in active regions as a possible mechanism for increasing the X-ray flaring activity in active stars (Güdel et al. 1997; Testa et al. 2004), in these stars this kind of interaction might be much less frequent, given the very sparse presence of active regions distributed over a large area.

In this paper for both the modeling and its interpretation, we have assumed that the quiescent emission is negligible with respect to the flaring emission. The *Chandra* observation does not provide a good grasp of the quiescent emission, as the hardness ratio behavior (and the emission measure distribution) suggests the presence of another dynamic event subsequent to the large flare (as in Reale et al. 2004). The *XMM-Newton* observations might represent the quiescent X-ray spectrum of HR 9024 without showing significant variability; however, their very low exposure times (6 and 3 ks) allow us only to assess the variability on very short timescales. Our preliminary results from a ~ 50 ks new *Suzaku* observation of HR 9024 shows extremely constant X-ray emission and provides an estimate of the quiescent X-ray luminosity and temperature of about 2×10^{31} ergs s $^{-1}$ and 3×10^7 K, respectively (P. Testa et al. 2007, in preparation), consistent with the findings based on *XMM-Newton* and *ROSAT* observations (Gondoin 2003; Singh et al.

1996). This X-ray luminosity value, which we assume is a good estimate for the quiescent emission of HR 9024, is about an order of magnitude lower than the peak luminosity of the flare observed with *Chandra*, therefore lending support to the assumption that the quiescent emission is negligible with respect to the flare emission. Also, the main results of our study rely on the emission of the very hot plasma, which is completely dominated by the flaring structure, and therefore they should not be significantly affected by ignoring the much cooler quiescent emission.

In this work we model the flare emission with a single loop structure, and it is worth discussing whether and to what extent very different solutions can be ruled out. We model the bulk of the flare where presumably there is one dominant loop structure, as observed in many compact solar flares occurring entirely in single loops and even in more complex flares, where one can often consider a dominant loop (e.g., Aschwanden & Alexander 2001). The single-loop model satisfactorily reproduces the *Chandra* observations analyzed in this work, and multiple-loop models would not add insight, but would include more free and unconstrained parameters. Furthermore, the single-loop model is supported by the fact that (1) the loop cross-sectional area is consistent with that of a single-loop structure; (2) the thermal distribution is compatible with that of a single flaring loop; and (3) the decay path in the density-temperature diagram has quite a steep slope (~ 2), implying negligible heating in the decay (Sylwester et al. 1993) and in turn indicating a single-loop structure, whereas flaring arcades are characterized by significant heating (e.g., Kopp & Poletto 1984). At later times of our observation (when the light curve rises again), other loops may be involved and become important in the evolution (e.g., Reale et al. 2004). The general expression of the loop length as a function of the observed decay time (eq. [1]) also allows us to estimate the uncertainties on the derived loop length. In particular, using the expression of the correction factor $f(\zeta)$ tuned for *Chandra*, as reported in Favata et al. (2005), we obtain $L_9 = 490$. Considering typical uncertainties of the diagnostic formula and the uncertainties on the observed temperature, we estimate an error of about 20%–30% on the loop length, therefore yielding $L = (4.9 \pm 1.5) \times 10^{11}$ cm. It is worth noting that this formula for estimating the uncertainties on the derived loop geometry assumes uniform heating and provides only approximate values for the loop length. The hydrodynamic model provides us with a much higher level of detail, giving us diagnostics for the temporal and spatial distribution of the heating, for the loop aspect, and for the thermal distribution of the plasma.

P. T. and D. P. H. were supported by SAO contract SV3-73016 to MIT for support of the *Chandra* X-Ray Center, which is operated by SAO for and on behalf of NASA under contract NAS8-03060. F. R. acknowledges support from Agenzia Spaziale Italiana and the Italian Ministero dell'Università e della Ricerca.

REFERENCES

- Aschwanden, M. J., & Alexander, D. 2001, *Sol. Phys.*, 204, 91
 Asplund, M., Grevesse, N., & Sauval, A. J. 2005, in *ASP Conf. Ser.* 336, *Cosmic Abundances as Records of Stellar Evolution and Nucleosynthesis*, ed. T. G. Barnes, III, & F. N. Bash (San Francisco: ASP), 25
 Audard, M., Telleschi, A., Güdel, M., Skinner, S. L., Pallavicini, R., & Mitra-Kraev, U. 2004, *ApJ*, 617, 531
 Ayres, T. R., Brown, A., Harper, G. M., Osten, R. A., Linsky, J. L., Wood, B. E., & Redfield, S. 2003, *ApJ*, 583, 963
 Ayres, T. R., Osten, R. A., & Brown, A. 1999, *ApJ*, 526, 445
 Ayres, T. R., Simon, T., Stern, R. A., Drake, S. A., Wood, B. E., & Brown, A. 1998, *ApJ*, 496, 428
 Betta, R., Peres, G., Reale, R., & Serio, S. 1997, *A&AS*, 122, 585
 Betta, R. M., Peres, G., Reale, F., & Serio, S. 2001, *A&A*, 380, 341
 Canizares, C. R., et al. 2000, *ApJ*, 539, L41
 ———. 2005, *PASP*, 117, 1144
 Cargill, P. J., & Klimchuk, J. A. 2006, *ApJ*, 643, 438
 Ciaravella, A., Peres, G., Maggio, A., & Serio, S. 1996, *A&A*, 306, 553
 de Medeiros, J. R., & Lebre, A. 1992, *A&A*, 264, L21

- Dere, K. P., Landi, E., Mason, H. E., Monsignori Fossi, B. C., & Young, P. R. 1997, *A&AS*, 125, 149
- Drake, J. J., Peres, G., Orlando, S., Laming, J. M., & Maggio, A. 2000, *ApJ*, 545, 1074
- Dupree, A. K., Brickhouse, N. S., Doschek, G. A., Green, J. C., & Raymond, J. C. 1993, *ApJ*, 418, L41
- Favata, F., Flaccomio, E., Reale, F., Micela, G., Sciortino, S., Shang, H., Stassun, K. G., & Feigelson, E. D. 2005, *ApJS*, 160, 469
- Favata, F., Micela, G., Reale, F., Sciortino, S., & Schmitt, J. H. M. M. 2000, *A&A*, 362, 628
- Flower, P. J. 1996, *ApJ*, 469, 355
- Gabriel, A. H. 1976, *Philos. Trans. R. Soc. London, A*, 281, 339
- García-Alvarez, D., Drake, J. J., Ball, B., Lin, L., & Kashyap, V. L. 2006, *ApJ*, 638, 1028
- Gondoin, P. 1999, *A&A*, 352, 217
- . 2003, *A&A*, 409, 263
- Griffiths, N. W., & Jordan, C. 1998, *ApJ*, 497, 883
- Güdel, M., Guinan, E. F., & Skinner, S. L. 1997, *ApJ*, 483, 947
- Haisch, B., & Schmitt, J. H. M. M. 1994, *ApJ*, 426, 716
- Kashyap, V., & Drake, J. J. 1998, *ApJ*, 503, 450
- . 2000, *Bull. Astron. Soc. India*, 28, 475
- Kopp, R. A., & Poletto, G. 1984, *Sol. Phys.*, 93, 351
- Landi, E., Del Zanna, G., Young, P. R., Dere, K. P., Mason, H. E., & Landini, M. 2006, *ApJS*, 162, 261
- Litwin, C., & Rosner, R. 1993, *ApJ*, 412, 375
- Ness, J.-U., Güdel, M., Schmitt, J. H. M. M., Audard, M., & Telleschi, A. 2004, *A&A*, 427, 667
- Nordon, R., & Behar, E. 2007, *A&A*, 464, 309
- Orlando, S., Peres, G., Reale, F., Rosner, R., & Siegel, A. 2003, *Mem. Soc. Astron. Italiana*, 74, 643
- Osten, R. A., Drake, S., Tueller, J., Cummings, J., Perri, M., Moretti, A., & Covino, S. 2007, *ApJ*, 654, 1052
- Peres, G., Orlando, S., Reale, F., Rosner, R., & Hudson, H. 2000, *ApJ*, 528, 537
- Peres, G., Reale, F., Serio, S., & Pallavicini, R. 1987, *ApJ*, 312, 895
- Peres, G., Serio, S., Vaiana, G. S., & Rosner, R. 1982, *ApJ*, 252, 791
- Perryman, M. A. C., et al. 1997, *A&A*, 323, L49
- Pizzolato, N., Maggio, A., & Sciortino, S. 2000, *A&A*, 361, 614
- Reale, F. 2002, in *ASP Conf. Ser. 277, Stellar Coronae in the Chandra and XMM-Newton Era*, ed. F. Favata & J. J. Drake (San Francisco: ASP), 103
- Reale, F., Betta, R., Peres, G., Serio, S., & McTiernan, J. 1997, *A&A*, 325, 782
- Reale, F., Bocchino, F., & Peres, G. 2002, *A&A*, 383, 952
- Reale, F., Güdel, M., Peres, G., & Audard, M. 2004, *A&A*, 416, 733
- Reale, F., Peres, G., Serio, S., Rosner, R., & Schmitt, J. H. M. M. 1988, *ApJ*, 328, 256
- Rosner, R., Tucker, W. H., & Vaiana, G. S. 1978, *ApJ*, 220, 643
- Sanz-Forcada, J., Brickhouse, N. S., & Dupree, A. K. 2002, *ApJ*, 570, 799
- Scelsi, L., Maggio, A., Peres, G., & Gondoin, P. 2004, *A&A*, 413, 643
- Schmitt, J. H. M. M., & Favata, F. 1999, *Nature*, 401, 44
- Schrijver, C. J., Lemen, J. R., & Mewe, R. 1989, *ApJ*, 341, 484
- Serio, S., Peres, G., Vaiana, G. S., Golub, L., & Rosner, R. 1981, *ApJ*, 243, 288
- Singh, K. P., Drake, S. A., White, N. E., & Simon, T. 1996, *AJ*, 112, 221
- Smith, R. K., Brickhouse, N. S., Liedahl, D. A., & Raymond, J. C. 2001, *ApJ*, 556, L91
- Sylwester, B., Sylwester, J., Serio, S., Reale, F., Bentley, R. D., & Fludra, A. 1993, *A&A*, 267, 586
- Testa, P., Drake, J., & Peres, G. 2004, *ApJ*, 617, 508
- Testa, P., Garcia-Alvarez, D., Reale, F., & Huenemoerder, D. 2006, in *Proc. The X-Ray Universe 2005*, ed. A. Wilson (ESA SP-604, Vol. 1; Noordwijk: ESA), 117
- Testa, P., Peres, G., & Reale, F. 2005, *ApJ*, 622, 695
- Vaiana, G. S., et al. 1981, *ApJ*, 245, 163